Vertically grown ultrathin Bi$_2$SiO$_5$ as high-κ single-crystalline gate dielectric

Jiabiao Chen [1], Zhaochao Liu[1], Xinyue Dong[1], Zhansheng Gao[1], Yuxuan Lin[1], Yuyu He[1], Yingnan Duan[1], Tonghuai Cheng[1], Zhengyang Zhou[2], Huixia Fu[3], Feng Luo[1] & Jinxiong Wu [1] ✉

Single-crystalline high-κ dielectric materials are desired for the development of future two-dimensional (2D) electronic devices. However, curent 2D gate insulators still face challenges, such as insufficient dielectric constant and difficult to obtain free-standing and transferrable ultrathin films. Here, we demonstrate that ultrathin Bi$_2$SiO$_5$ crystals grown by chemical vapor deposition (CVD) can serve as excellent gate dielectric layers for 2D semiconductors, showing a high dielectric constant (>30) and large band gap (~3.8 eV). Unlike other 2D insulators synthesized via in-plane CVD on substrates, vertically grown Bi$_2$SiO$_5$ can be easily transferred onto other substrates by polymer-free mechanical pressing, which greatly facilitates its ideal van der Waals integration with few-layer MoS$_2$ as high-κ dielectrics and screening layers. The Bi$_2$SiO$_5$ gated MoS$_2$ field-effect transistors exhibit an ignorable hysteresis (~3 mV) and low drain induced barrier lowering (~5 mV/V). Our work suggests vertically grown Bi$_2$SiO$_5$ nanoflakes as promising candidates to improve the performance of 2D electronic devices.

Two-dimensional (2D) semiconductors hold great promise for fabricating more-than-Moore transistors and exploring the emergent transport properties[1–5], but achieving their theoretical performance also requires compatible high-k dielectrics to guarantee efficient gate control[6–10]. Compared to traditional amorphous dielectrics (Al$_2$O$_3$ and HfO$_2$)[11–13], single-crystalline gate insulators with dangling-bond-free surfaces are more competitive to fabricate high-performance 2D devices with reduced interfacial scatterings and gate hysteresis[14–18]. For example, hexagonal boron nitride (h-BN) has been widely used as a van der Waals (vdWs) substrate to improve carrier mobility and investigate exotic properties of 2D materials[19–23]. However, h-BN is also well known for its shortcomings of low dielectric constant ($k = 2$-4) and harsh conditions (pressure: >4 G Pa, temperature: >1673 K) for the growth of high-quality single crystals[24]. Therefore, it is highly desirable to discover new vdWs insulators similar to h-BN, but has a much higher dielectric constant and more facile synthetic conditions, for exploring

the emergent transport properties of 2D materials in a high-κ dielectric environment, as well as for fabricating 2D-material-based electronic devices with scaled supply voltage[15,16]. Even so, very rare have succeeded[18,25]. Very recently, Peng et al.[18] reported the synthesis of Bi$_2$SeO$_5$ bulk crystals grown by chemical vapor transport (CVT), which can be exfoliated into few-nanometer-thick nanosheets and serve as an "h-BN" like high-κ dielectric to improve the mobility of 2D materials and enable the observation of quantum Hall effects in Bi$_2$O$_2$Se. Nevertheless, the CVT process for the synthesis of Bi$_2$SeO$_5$ bulk crystals is also very time-consuming (typically ~40 days). Besides, similar to other vdWs dielectrics, transferable Bi$_2$SeO$_5$ nanoflakes with suitable thicknesses and domain sizes were also prepared by a low-efficiency method of mechanical exfoliation for subsequent vdWs device integration.

Compared to mechanical exfoliation, direct growth of free-standing ultrathin 2D insulators with high-k nature by chemical

[1]Tianjin Key Lab for Rare Earth Materials and Applications, Center for Rare Earth and Inorganic Functional Materials, Smart Sensor Interdisciplinary Science Center, School of Materials Science and Engineering, Nankai University, Tianjin 300350, China. [2]State Key Laboratory of High Performance Ceramics and Superfine Microstructure, Shanghai Institute of Ceramics, Chinese Academy of Sciences, Shanghai 200093, China. [3]Center of Quantum Materials and Devices & College of Physics, Chongqing University, Chongqing 401331, China. ✉e-mail: jxwu@nankai.edu.cn

vapor deposition (CVD) is much more efficient, but remains challenging. Typically, CVD-grown atomically thin 2D insulators with a layered crystal structure preferably adopt an in-plane growth mode on substrates[26–29], which will inevitably set obstacles for clean sample transfer and subsequent vdWs integration. However, if an ultrathin 2D insulator can be vertically grown on the substrate, just like the case in Bi_2O_2Se[3,30,31], the transfer problem can be easily overcome due to much reduced interfacial interaction.

Bi_2SiO_5 is a well-known high-κ dielectrics with an Aurivillius-type layered structure and a large band gap of 3.5-4.4 eV[32–35]. According to the previous works regarding the bulk single crystals and poly-crystalline powders of Bi_2SiO_5, Bi_2SiO_5 shows an anisotropic dielectric constant[36,37] and its out-of-plane dielectric constant can be as high as 30-80[36–39], and thus was suggested as a potential candidate for high-temperature dielectrics[39]. Here, Bi_2SiO_5 was demonstrated as an excellent gate dielectric for 2D semiconductors. Ultrathin Bi_2SiO_5 single crystals with thickness down to monolayer were successfully synthesized by a facile CVD method, concurrently owing to the high dielectric constant (>30), large band gap (~3.8 eV), and large breakdown field strength. Remarkably, the preferable CVD growth mode of Bi_2SiO_5 can be regulated from in-plane to out-of-plane under optimized conditions, showing great feasibility on sample transfer by polymer-free mechanical pressing. Using ultrathin Bi_2SiO_5 nanoflakes as the vdW dielectrics and screening layers, we can greatly regulate the carrier density and improve the carrier mobility of few-layer MoS_2 (almost fifteen times higher than on the SiO_2 substrate at 5 K). Besides, the MoS_2 field-effect transistors (FETs) using Bi_2SiO_5 as dielectrics can operate at 0.5 V, exhibiting a large I_{on}/I_{off} (>10[8]), an ignorable hysteresis (~3 mV), low DIBL value (~5 mV/V) and low gate leakage current (~10[-13] A).

Results

Structure, CVD growth, and characterization of layered Bi_2SiO_5

As shown in Fig. 1a, bismuth silicate Bi_2SiO_5 possesses a monoclinic lattice with Cc space group (quasi-orthogonal, $a = 15.12$ Å, $b = 5.44$ Å, $c = 5.29$ Å, $\beta = 90.07°$) and has an Aurivillius-type layered crystal structure with alternatively stacked $[Bi_2O_2]_n^{2n+}$ and $[SiO_3]_n^{2n-}$ layers along the a-axis. The first-principle calculations were performed to investigate the band structure of layered Bi_2SiO_5. As shown in Fig. 1b, Bi_2SiO_5 exhibits a large direct band gap of ~3.79 eV, whose conduction band minimum (CBM) and valance band maximum (VBM) are both locate at Γ point of the first Brillouin zone and mainly originate from Bi-p and O-p orbits, respectively.

The essential prerequisite for using Bi_2SiO_5 as single-crystalline dielectrics with strong gate control is to achieve its growth of atomically thin films. However, the CVD growth of ultrathin Bi_2SiO_5 crystals remains a challenge yet. To our knowledge, SiO_2 is chemically inert and has a very high melting point, which prevents it to be used as Si supplier during the CVD growth of Si-based compounds to some extent. Nevertheless, it's well known that the fluorides will react with SiO_2 to form volatile Si-based precursors. As a result, we developed a facile CVD method for the synthesis of Bi_2SiO_5 ultrathin crystals by using the BiF_3 powders as Bi supplier and SiO_2 powders or quartz boat as Si supplier (see Supplementary Fig. 1). With this method, ultrathin Bi_2SiO_5 crystals with various thicknesses can be readily obtained on mica substrates. As shown in Fig. 1c, d and Supplementary Fig. 2, at a relatively high growth temperature (~1023 K), Bi_2SiO_5 adopts a preferable in-plane growth mode on mica, which is widely observed in the CVD synthesis of layered materials, revealing a transparent square-like shape and atomically thin nature (down to monolayer, Supplementary Fig. 3). Normally, the in-plane growth mode will result in a large attaching area and strong bonding force between the epitaxial layer and the substrate, thereby adding difficulties for sample transfer and subsequent vdWs integration. Remarkably, the preferable growth mode of Bi_2SiO_5 on mica can be regulated from in-plane to out-of-

plane growth modes just by lowering its growth temperature, which is similar to the case of Bi_2O_2Se[30]. As shown in Fig. 1e and Supplementary Fig. 2b, c, vertically grown ultrathin Bi_2SiO_5 crystals gradually emerge on mica at ~973 K, then dominates the CVD growth while further lowering the temperature to ~923 K. Unlike the case in Fig. 1c, vertically grown Bi_2SiO_5 crystals with thickness ranging from 7.5 to 50 nm can be easily transferred onto various substrates (such as SiO_2/Si, Fig. 1e) by a polymer-free mechanical pressing (Supplementary Fig. 4), showing an atomically flat surface even after sample transfer (Fig. 1f). The transferable feature without unfavorable residual polymer contaminations makes free-standing Bi_2SiO_5 appealing for fabricating vdWs heterojunction device. Occasionally, the CVD-grown Bi_2SiO_5 nanoflakes revealed a terraced morphology with a step height of ~0.76 nm (Fig. 1g), consistent with the theoretical value for the monolayer step in Bi_2SiO_5. It's worth noting that the CVD-grown Bi_2SiO_5 shows excellent air stability, whose surface morphology and roughness of Bi_2SiO_5 nanoplates remain almost the same when exposed to air for more than 7 months, which is an important metric for device fabrication as a high-κ gate dielectric (Supplementary Figs. 5, 6). More details about the comparison experiments conducted to understand how the reaction goes in the CVD growth of Bi_2SiO_5 and the possible reason for its in-plane and out-of-plane growth can be found in the discussion part of supporting information (Supplementary Figs. 7, 8).

The crystalline phase of as-grown samples was confirmed by transmission electron microscopy (TEM), Raman spectroscopy, and X-ray diffraction (XRD). As shown in Fig. 1h, i and Supplementary Fig. 9, we performed high-resolution TEM imaging along three-zone axes [namely (010), (011), and (100)], as well as corresponding fast Fourier transform (FFT) fringes. Based on the atomic-resolved cross-sectional TEM technique, the alternative stacking of $[Bi_2O_2]_n^{2n+}$ and the $[SiO_3]_n^{2n-}$ layers with a layer space of 0.76 nm was observed. Besides, the averaged atomic ratio of Bi/Si was measured close to 2: 1 by energy dispersive spectroscopy (EDS, Supplementary Figs. 9, 10), which is consistent with the chemical formula of Bi_2SiO_5. The active modes at 70, 97, 149, 208, 298, 372, 433 cm^{-1} of the Raman spectra also matched well with monoclinic Cc phase of Bi_2SiO_5 (Supplementary Fig. 11)[35]. Additionally, the sharp XRD peaks, which can be assigned to (h00) crystal planes, further confirmed the high crystalline quality of the CVD-grown Bi_2SiO_5 nanoplates (Supplementary Fig. 11c).

Dielectric properties of vertically grown Bi_2SiO_5 nanoplates

The transfer feasibility for vertically grown Bi_2SiO_5 nanoplates greatly facilitates the evaluation of their intrinsic properties, such as dielectric constant, band gap, and breakdown field strength. As shown in Fig. 2a, metal-insulator-metal (MIM) capacitors were fabricated on quartz substrates to extract the dielectric constant of Bi_2SiO_5 nanoflakes with varied thicknesses by capacitance-voltage ($C–V$) measurements. Here, the thick graphite and In/Au metals serve as the bottom and top electrodes, respectively. Thanks to high-κ nature, Bi_2SiO_5 nanoflake with a thickness of 25.6 nm demonstrated a very high capacitance density of 1.12 $\mu F/cm^2$ at 100 Hz (Fig. 2a), revealing a slight decrease when the measuring frequency is up to 1 MHz. The corresponding capacitance-frequency ($C–f$) measurements showed the similar results (Fig. 2b). It is worth noting that the absolute capacitance value (>1 × 10^{-12} F) measured is ~2-3 orders higher than the instrument's offset and noise level (<1.5 × 10^{-14} F, Supplementary Fig. 12). Based on the $C–V$ and $C–f$ data, we can estimate the effective permittivity (ε_{eff}) of Bi_2SiO_5 to be ~32.4 at 100 Hz, which is preferable than commercial amorphous high-κ oxide such as Al_2O_3 ($k = 7$-9)[13,40,41] and HfO_2 ($k = 13$-17)[41,42], and higher than most of reported vdWs single-crystalline dielectrics, such as h-BN ($k = ~3.5$)[43,44], CaF_2 ($k = 8.4$)[14], Bi_2SeO_5 ($k = 15.6$)[18], VOCl ($k = 11.7$)[45] and ZrO_2 ($k = 8$-19)[17]. Furthermore, we investigated the thickness-dependent ε_{eff} by fabricating MIM capacitors with different Bi_2SiO_5 thicknesses, from which we can extract very large ε_{eff} values of >30 in a wide thickness range (Fig. 2c).
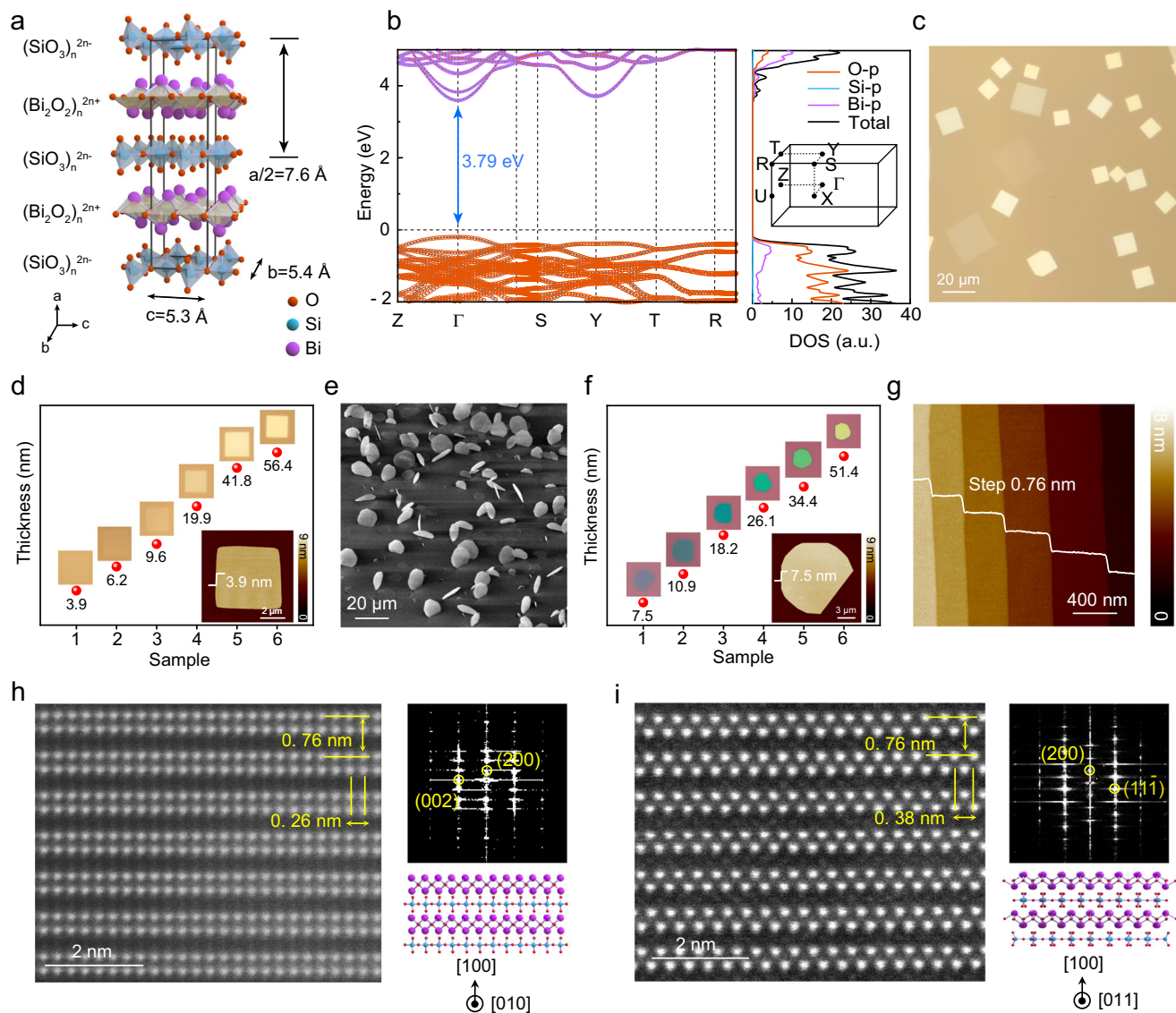
Fig. 1 | Structure, growth, and characterization of ultrathin Bi₂SiO₅ single crystals. a Crystal structure of Bi_2SiO_5 (Cc, $a = 15.12$ Å, $b = 5.44$ Å, $c = 5.29$ Å, $\beta = 90.07°$) with alternatively stacked $[Bi_2O_2]_n^{2n+}$ and $[SiO_3]_n^{2n-}$ layers. **b** Calculated band structure and density of states (DOS) of Bi_2SiO_5 with a direct band gap of ~3.79 eV. The first Brillouin zone is inserted in the right panel. **c** Typical optical micrograph (OM) image of square Bi_2SiO_5 nanoplates showing an in-plane growth mode on mica substrate. **d** OM images of Bi_2SiO_5 nanoplates with thickness-dependent color contrasts on mica. The inset shows the typical atomic force microscope (AFM) image of an ultrathin Bi_2SiO_5 nanoplate with a thickness of 3.9 nm (5 layers) and an atomically smooth surface. **e** Scanning electron microscopy (SEM) image of 2D Bi_2SiO_5 crystals vertically grown on mica substrate. **f** Thickness-dependent color contrasts for Bi_2SiO_5 nanoplates transferred onto SiO_2/Si substrate by a polymer-free mechanical pressing. The AFM image of a 7.5-nm-thick Bi_2SiO_5 nanoplate was inserted in **f**. **g** Typical AFM image of a terraced Bi_2SiO_5 nanoplates with a clear step of 0.76 nm. **h, i** Cross-sectional atomic-resolved high angle annular dark field (HAADF) images (left) and corresponding fast Fourier transform (FFT) diffraction spots (right) of chemical vapor deposition (CVD) grown Bi_2SiO_5 nanoplates taken along the zone axes of [010] (**h**) and [011] (**i**), respectively.

The gradual decrease of ε_{eff} while thinning down can be ascribed to the existence of interfacial "dead layer" in the MIM device, which is similar to other MIM devices[15,46–48].

An ideal gate dielectric also needs a large band gap to inhibit the current leakage. Here, vertically grown Bi_2SiO_5 nanoflakes were directly transferred onto the polished quartz substrate by mechanical pressing for the ultraviolet-visible (UV-vis) absorption measurements. As shown in Fig. 2d, the optical band gap of CVD-grown Bi_2SiO_5 can be extracted as ~3.80 eV by Tauc's law, which is consistent with the theoretical value (3.79 eV, Fig. 1b). To illustrate the metrics of Bi_2SiO_5 as a gate dielectric, the relationship between band gap and dielectric constant of representative gate dielectrics in literature was plotted in Fig. 2e, clearly indicating the coexistence of high dielectric constant and large band gap in Bi_2SiO_5. Moreover, we evaluated the breakdown

field strength (E_{bd}) of the Bi_2SiO_5 nanoplates by conductive atomic force microscope (C-AFM) measurements on p⁺⁺ Si. As shown in Fig. 2f, the CVD-grown Bi_2SiO_5 showed thickness-dependent breakdown field strength ranging from 7.2 (13.5 nm) to 9.4 (8.2 nm) MV cm⁻¹, which is close to that of dielectrics in the silicon industry such as Al_2O_3[49] and HfO_2[50] but owns higher dielectric constant. We should emphasize that the C-AFM is a very local and microscopic tool to measure the breakdown voltage of a dielectric insulator, which may be not the same as the global one determined by MIM device. For example, the breakdown experiments based on the MIM devices gave a breakdown field strength of 3-5 MV/cm instead while varying the thickness of Bi_2SiO_5 from 10.1 to 21.4 nm (Supplementary Fig. 13).

The features of easy-to-transfer, ultra-flat surface, high dielectric constant, large band gap, and breakdown field strength make Bi_2SiO_5
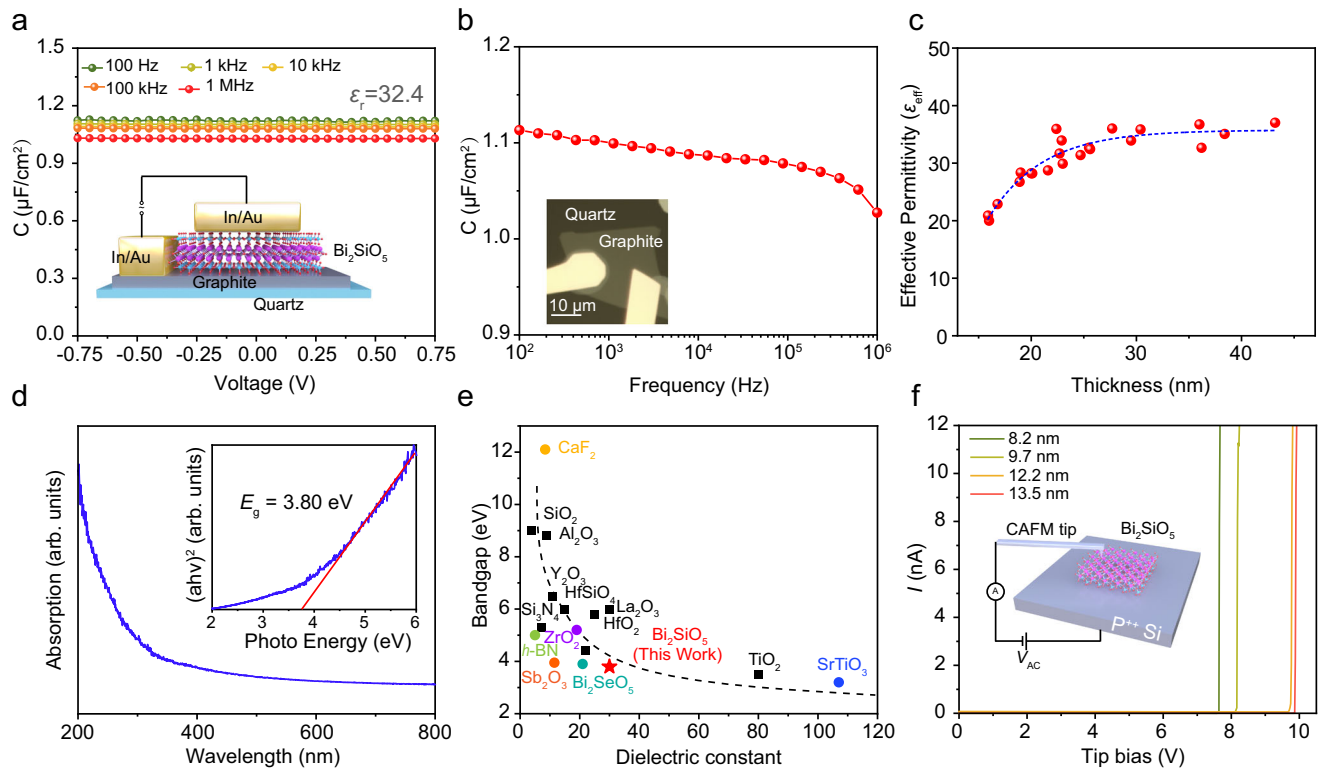
Fig. 2 | Dielectric constant, band gap, and breakdown field strength of CVD-grown Bi_2SiO_5 nanoflakes. a Typical Bias-dependent capacitance (C) measurements on CVD-grown Bi_2SiO_5 nanoflake with a common metal-insulator-metal (MIM) device configuration, where the thick graphite and In/Au metals serve as the bottom and top electrodes (inset), respectively. The dielectric constant (ε_r) of Bi_2SiO_5 was estimated as ~32.4 at 100 Hz. **b** Corresponding frequency-dependent capacitance (C–f) characteristics of the MIM device, whose OM image is inset in **b**. **c** The thickness-dependent effective permittivity (ε_{eff}) of Bi_2SiO_5 nanoflakes with a measuring frequency of 100 Hz. The dashed blue curve is a visual guide. **d** Ultraviolet-visible (UV-vis) absorption spectrum of CVD-grown Bi_2SiO_5 nanoflakes transferred onto quartz substrate with high coverage by mechanical pressing. The inset shows the fitting of its optical band gap (~3.8 eV) by Tauc's law, where a, h, and v are the absorption coefficient, Planck constant and frequency, respectively. **e** Energy band gap versus dielectric constant of representative dielectric materials in literature, showing the coexistence of high dielectric constant and large band gap in Bi_2SiO_5. The dashed line is a visual guide. **f** Thickness-dependent current-voltage curves of Bi_2SiO_5 nanoplates measured by C-AFM, showing a high breakdown field strength of 9.4 MV/cm (8.2 nm).

highly competitive as gate dielectrics and high-κ substrates for dielectric screening. Here, we combine Bi_2SiO_5 with mechanically exfoliated few-layer MoS_2 to construct Bi_2SiO_5/MoS_2 FETs for demonstrating its advantages as back-gate dielectrics (Fig. 3), dielectric screening substrate (Fig. 4) and top-gate dielectrics (Fig. 5).

Vertically grown Bi_2SiO_5 as back-gate dielectric

The small contact area and weak interaction between the vertically grown Bi_2SiO_5 and the mica substrate make it compatible with the well-developed aligned transfer method (For details, see Supplementary Fig. 14)[19,20], allowing us to fabricate complex vdWs heterojunction devices by layer-by-layer stacking. Figure 3a showed the OM image of an as-fabricated MoS_2 Hall-bar device using Bi_2SiO_5 as the back-gate dielectric and multi-layer graphene as a back-gate electrode. Gated Hall measurement is a powerful tool to get a series of key parameters, such as the dielectric constant of the gate dielectric, carrier density, and Hall mobility of the channel semiconductor. Besides, it also enables us to get the transfer and output characteristics by defining two out of six electrodes as source and drain. Figure 3b showed Hall resistance (R_{xy}) as a function of magnetic field (B) under different gate voltages (V_g) at room temperature, from which we can extract the V_g-dependent sheet carrier densities (n_{2D}). By linear fitting the curve of n_{2D}-V_g (Fig. 3c), the estimated slope equals the C_{ox}/e, where C_{ox} is capacitance density and e is the elementary charge. The C_{ox} for a 22-nm-thick Bi_2SiO_5 can be as high as 1.45 µF/cm², suggesting a very high dielectric constant (ε_r ~ 36), which is consistent with the value extracted by C–V measurements in a reasonable accuracy. On the other hand, the

very large capacitance density suggests that we can greatly regulate the carrier density and electrical behavior of the MoS_2 semiconductor. As confirmed by the room-temperature Hall measurements (Fig. 3c), a very high carrier density of 1.83×10^{13} cm⁻² can be doped into the channel by applying a V_g of 2 V on Bi_2SiO_5 dielectrics. To this end, the temperature-dependent longitudinal resistance (R_{xx}-T) behavior of MoS_2 can be greatly regulated from insulating to metallic one when sweeping the V_g from 0.4 to 2 V (Fig. 3d), indicating the great potential of Bi_2SiO_5 dielectric as a powerful tool for physical state regulation.

To examine whether ultrathin Bi_2SiO_5 can serve as excellent back-gate dielectrics of a FET, we define the electrodes #1, #4 and graphene as source, drain, and gate electrodes, respectively. The dual-sweep transfer curves of $MoS_2/Bi_2SiO_5/Gr$ FET were presented in Fig. 3e, showing a large I_{on}/I_{off} of >10⁸, and a small SS value of ~64 mV/decade. Considering the relatively complex device fabrication process (Supplementary Fig. 14), chemical residuals will inevitably remain at the interfaces between the graphene, Bi_2SiO_5 and MoS_2, which are detrimental to the device performance. Nevertheless, the FET still exhibited small hysteresis of ~15 mV, which is comparable to the value obtained after interface optimization[51]. Thanks to the Ohmic contact formed by In/Au electrodes (Fig. 3f), two-terminal field-effect mobility of the device can be as high as 18.6 cm² V⁻¹ s⁻¹ by linear fitting the transfer curve, which is comparable to the Hall mobility measured at room temperature (23.7 cm² V⁻¹ s⁻¹ at V_g = 2 V, Supplementary Fig. 15). Notably, Bi_2SiO_5 was also verified as an excellent gate insulator while shrinking the channel length of MoS_2 FETs down to 100 nm and even 30 nm (Supplementary Figs. 16, 17).
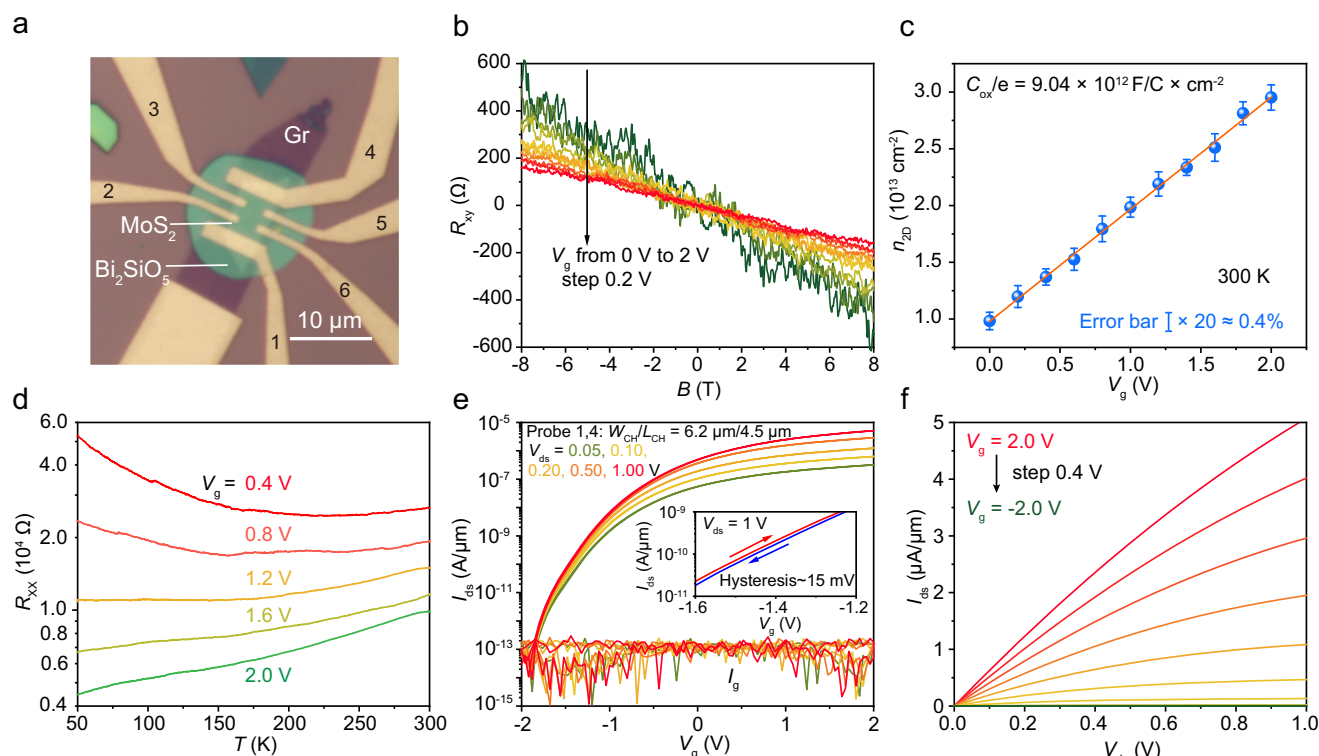
Fig. 3 | MoS₂ Hall-bar device with the vertically grown ultrathin Bi₂SiO₅ nanoflake as the high-κ back-gate dielectrics. a OM image of an as-fabricated MoS₂ (-2.7 nm) Hall-bar device on SiOₓ/Si substrate, in which a thin flake of Bi₂SiO₅ (-22 nm) and multi-layer graphene were adopted as gate dielectric and back-gate electrode, respectively. **b** Hall resistance (R_{xy}) as a function of magnetic field (B) under various gate voltages (V_g) from 0 to 2 V at 300 K. **c** The extracted V_g-dependent sheet carrier density (n_{2D}), in which a high dielectric constant (ε_r) of -36 was derived by linear fitting. The Error bars are based on the standard deviations of slope fitting on R_{xy}-B curves. **d** Longitudinal resistance (R_{xx}) as a function of temperature (T) under different V_g from 0.4 to 2.0 V, showing a gate-induced insulator-to-metal transition. **e** Two-probe transfer curves of the back-gated MoS₂/Bi₂SiO₅ field-effect transistor (FET) measured by defining the probes of 1 and 4 as source and drain terminals, showing $I_{on}/I_{off} > 10^8$, SS - 64 mV/decade. The inset shows a small hysteresis of -15 mV. The extracted two-terminal field-effect mobility of the device is 18.6 cm² V⁻¹ s⁻¹. **f** The corresponding output curves measured in a V_g range from 2 to −2 V.

## Vertically grown Bi₂SiO₅ as high-κ screening layer

Dangling bonds on SiO₂/Si substrate usually act as the scattering sites of Coulomb impurities (CI) to decrease the mobility of a semiconductor[52–54]. Theoretically speaking, using an *h*-BN-like high-κ substrate free of dangling bonds can effectively enhance its mobility due to reduced CI scatterings and excellent dielectric screening. Figure 4a shows the scheme and OM image of as-fabricated 4-probe MoS₂ FETs on top of Bi₂SiO₅ and SiO₂/Si substrates. To avoid the influence of sample quality variation, one MoS₂ sample (4.3 nm) was simultaneously placed on Bi₂SiO₅ (31.9 nm) and SiO₂ substrates for comparison. As demonstrated in Fig. 4b, the V_g-dependent two-probe *I*−*V* curves (output characteristics) were measured at 300 K, showing a linear behavior over a large voltage window, confirming the Ohmic contact formed by In/Au electrodes. It's worth noting that the on-state current (I_{on}) of MoS₂ on Bi₂SiO₅ is about twice as the one on SiO₂, suggesting a higher mobility of MoS₂ on Bi₂SiO₅ substrate. To illuminate the influence of contact resistance, 4-probe transfer curves were measured among a temperature range of 5-300 K (Fig. 4c). By linear fitting the transfer curves, we can extract the 4-probe FET mobility ($\mu_{FET,4\text{-}probe}$) as a function of temperature (Fig. 4d). Among the whole temperature range of 300-5 K, the carrier mobility of MoS₂ on Bi₂SiO₅ is significantly higher than that on SiO₂/Si substrate, which can be further confirmed by plotting the I_{ds} as a function of a normalized V_g by threshold voltage (V_g-V_{th}, Supplementary Fig. 18). Particularly, the mobility of MoS₂ on Bi₂SiO₅ at 5 K is as high as 549.3 cm² V⁻¹ s⁻¹, which is almost fifteen times higher than the value of MoS₂ on SiO₂/Si (-37.4 cm² V⁻¹ s⁻¹). Moreover, the carrier mobility of MoS₂ on Bi₂SiO₅ and SiO₂/Si showed totally different temperature dependence. For

MoS₂/Bi₂SiO₅, its carrier mobility increased monotonously upon cooling down, suggesting the phonon scattering dominated the whole transport events even at low temperature. In contrast, the carrier mobility of MoS₂ on SiO₂/Si substrate increased first while cooling down to -150 K, but gradually decreased upon further cooling. This *T*-dependent mobility can be well explained by enhanced charge impurities scattering at low temperature in MoS₂/SiO₂ interface. In a word, using Bi₂SiO₅ as a substrate greatly improve the performance of the MoS₂ FET to get a higher mobility, which can be attributed to the suppressed CI scatterings in the high-κ surroundings and ideal dielectric/semiconductor interface.

Vertically grown Bi₂SiO₅ as the top-gate dielectric

Top-gate FET is a widely used device configuration in practical applications. In this part, we fabricated Bi₂SiO₅/MoS₂ top-gate FETs to prove the feasibility of Bi₂SiO₅ as top-gate dielectric layer in hysteresis-free low-power transistors (Supplementary Fig. 19). As shown in Fig. 5a, the Bi₂SiO₅/MoS₂ top-gate FET was placed on the SiO₂/Si substrate, which can also serve as the back-gate dielectric and electrode when necessary. Figure 5b showed the typical dual-sweep transfer curves of a 22.9-nm-thick Bi₂SiO₅-based MoS₂ FET measured under different V_{ds} from 0.05 to 1 V. Owing to the excellent gate tunability, the transistor can be effectively turned on and off by applying a V_g within the range of −0.6-0.5 V, showing a large I_{on}/I_{off} of >10⁶ and a low gate leakage current of 10⁻¹³ A (approaching the detection limit). Furthermore, the ideal SS value (-62 mV/decade), ignorable gate hysteresis (-3 mV), and low drain-induced barrier lowering (DIBL, -5 mV/V) suggest the perfect interface was formed at MoS₂/Bi₂SiO₅ interface (Supplementary

a

b

c

d
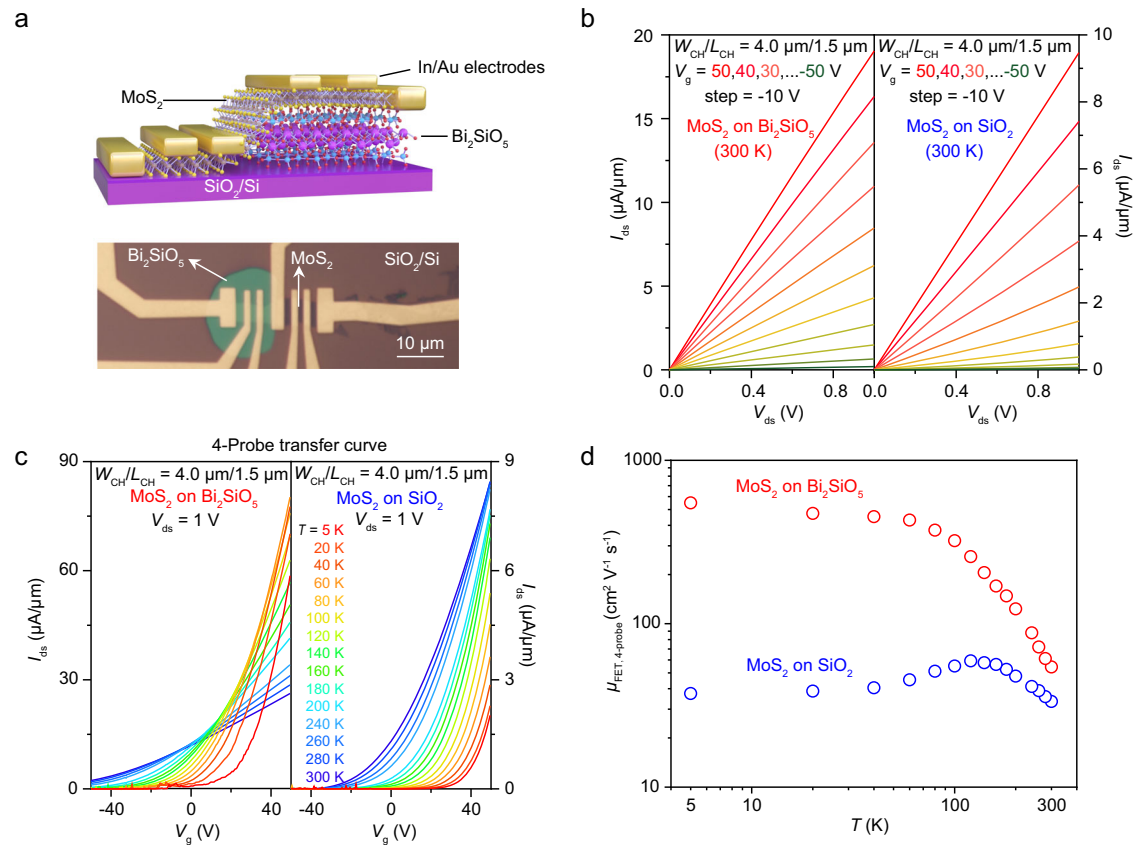
Fig. 4 | Dielectric screening and mobility enhancement effects of CVD-grown Bi$_2$SiO$_5$ nanoflakes as the high-κ substrates. a Schematic illustration and OM image of back-gate MoS$_2$ four-probe FETs device. **b** Linear output curves (I_{ds}–V_{ds}) of MoS$_2$ FETs on Bi$_2$SiO$_5$ (left) and on SiO$_2$ substrate (right) measured at 300 K. **c** The 4-probe transfer curves of MoS$_2$ FETs measured at different temperatures (5-300 K) on Bi$_2$SiO$_5$ (left) and SiO$_2$ (right) substrates, respectively. **d** The extracted temperature-dependent 4-probe FET mobility ($\mu_{FET,4\text{-}probe}$) of MoS$_2$ on Bi$_2$SiO$_5$ (red) and SiO$_2$ (blue) substrates.

Fig. 20). The MoS$_2$ transistor showed a linear I_{ds}-V_{ds} curve at low V_{ds} region, then gradually saturated at high V_{ds} region (Fig. 5c). Particularly, the SS remains low (<70 mV/decade) for different I_{ds} of several orders of magnitude for both forward and reverse top-gate sweeping (Fig. 5d). More importantly, the top-gate Bi$_2$SiO$_5$/MoS$_2$ short-channel FET, whose channel length was defined by the gap distance between two graphene electrodes (~180 nm), still showed a small DIBL value of ~22 mV/V and SS value of ~79 mV/decade (Supplementary Fig. 21).

One step further, nearly hysteresis-free transfer curves were preserved in a dual-gate FET configuration, in which a back-gate voltage (V_{BG}) was employed to modulate the threshold voltage (V_{th}) of the device. As a result, the top-gate transfer curves gradually shifted as the V_{BG} varied from 5 to 0 V (Fig. 5e and Supplementary Fig. 22). By linear fitting the V_{th} as a function of V_{BG}, we can extract a slope of −0.0097, which equals to the ratio of the bottom-gate to top-gate capacitance, namely $C(\text{SiO}_2)/C(\text{Bi}_2\text{SiO}_5)$, when the parallel-plate capacitor model is assumed for both top and bottom gates[16,55]. For a 285 nm SiO$_2$ dielectric ($\varepsilon_r = 3.9$), its capacitance can be calculated as 0.0121 μF/cm^2. In this case, the capacitance and dielectric constant for a 22.9-nm-thick Bi$_2$SiO$_5$ were derived as 1.25 μF/cm^2 and 32.3, both of which matched well with the value obtained by C–V (Fig. 2a) and gated Hall measurements (Fig. 3c). Next, the interface trap density D_{it} was extracted based on the following equation:[15]

$$SS = \ln(10)\frac{k_B T}{q}\left(1 + \frac{qD_{it}}{C_{ox}}\right) \qquad (1)$$

where SS is the subthreshold swing, k_B is Boltzmann constant, T is absolute temperature, q is the elementary charge, C_{ox} is the gate

capacitance obtained from MOS capacitance measurements. As a result, a low D_{it} value of 2.88×10^{11} cm^{-2}/eV was extracted, verifying the high quality of the vdWs interface.

Moreover, the dielectric constant of Bi$_2$SiO$_5$, extracted by dual-gate transfer measurements, also showed similar thickness dependence with the C–V results (Fig. 5g). Figure 5h plotted the dual-sweep transfer curves of MoS$_2$ FETs with different Bi$_2$SiO$_5$ thicknesses (10.1-67.5 nm). Apparently, smaller V_g is needed to switch the transistor on and off when a thinner Bi$_2$SiO$_5$ dielectric is used. We should emphasize that the EOT value for a 10.1 nm Bi$_2$SiO$_5$ is as small as 1.3 nm, but its gate leakage current is still on the order of 10^{-13} A, signifying substantial room space for further scaling of EOT and great potential applications in low-power devices. The I_{on} of MoS$_2$ FETs in Fig. 5h seems to decrease with decreasing the thickness of Bi$_2$SiO$_5$, which may originate from the contact issues existing in the MoS$_2$ FETs with the thin Bi$_2$SiO$_5$ as gate insulators. However, we should emphasize that, the I_{on} of ultrathin Bi$_2$SiO$_5$-gated MoS$_2$ FETs can be greatly improved by optimizing the device fabrication process. As shown in Supplementary Figs. S23−25, the I_{on} of another 10-nm-thick Bi$_2$SiO$_5$-gated MoS$_2$ can be similar to the value of the thick Bi$_2$SiO$_5$-gated FETs (0.11 μA/μm, Fig. 5b). It is worth noting that the I_{on} is greatly limited by the remaining ungated channel in the top-gate device configuration. Additionally, as confirmed by the dual-sweep transfer curves, a nearly ideal SS value and a low normalized gate hysteresis can indeed be obtained in the Bi$_2$SiO$_5$ gated MoS$_2$ FET.

The low operating voltage is essential to fabricate low-power logic circuits. As demonstrated in Fig. 5i, we used two n-type transistors as the load and driver terminal to construct 2D inverter with a high voltage gain of 22.0. The inverter can demonstrate the logic state 0 and 1
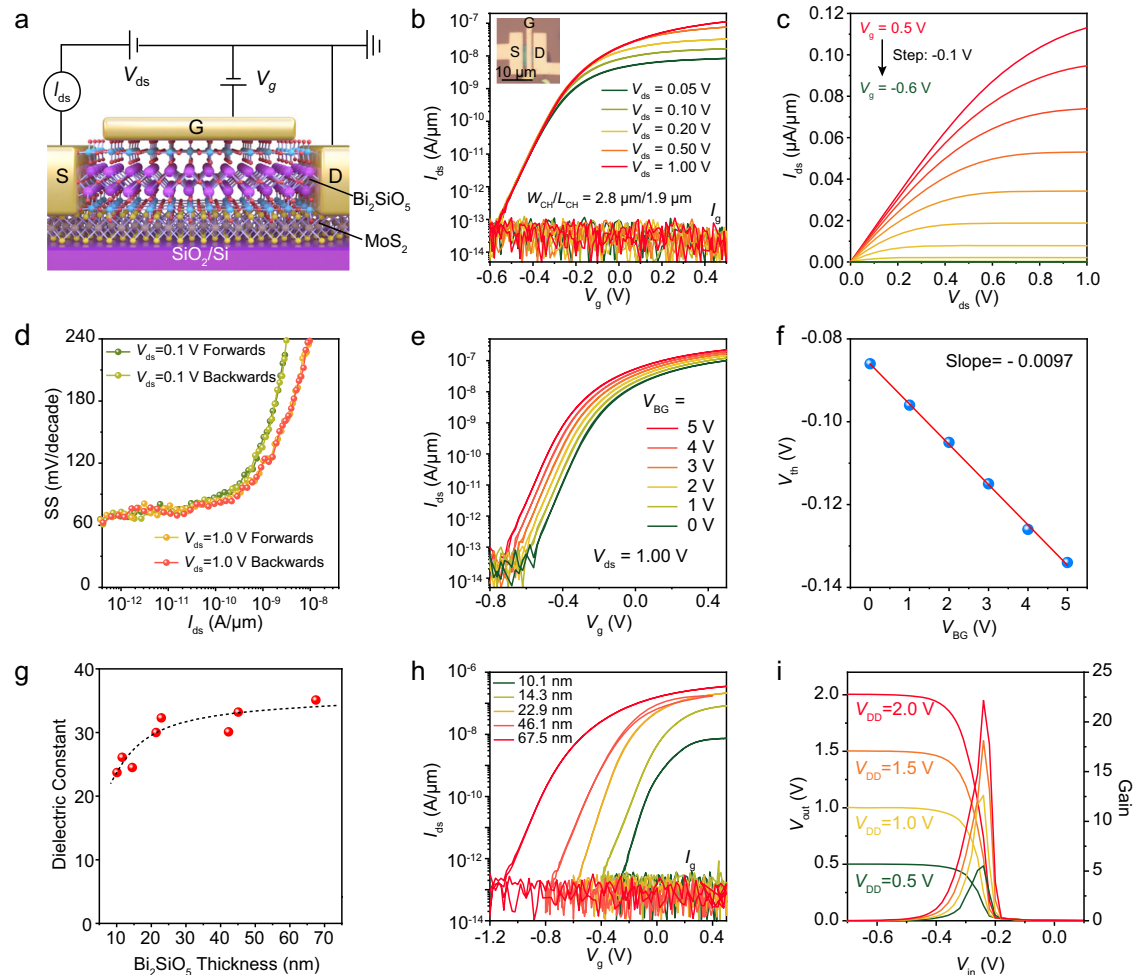
Fig. 5 | Hysteresis-free MoS₂ FETs and low-power NMOS inverters using Bi₂SiO₅ as high-κ top-gate dielectrics. a Schematic illustration of the top-gated MoS₂ FETs on SiO₂/Si substrate with Bi₂SiO₅ as the top-gate dielectric. **b** Typical dual-sweep transfer curves of the MoS₂/Bi₂SiO₅ FET measured under different V_{ds} from 0.05 to 1 V, showing an ideal *SS* value of ~62 mV/decade and ignorable gate hysteresis. The Insert is the OM image of a fabricated MoS₂ FET with Bi₂SiO₅ as the gate dielectric. **c** Corresponding output characteristics (I_{ds}–V_{ds} curves) of the device measured by varying the V_g from 0.5 to −0.6 V with a 0.1 V step. **d** Extracted *SS* value versus I_{ds} characteristics of the device in **b**, showing a low SS value (<70 mV/decade) for a wide I_{ds} range. **e** Dual gated transfer curves of the MoS₂/ Bi₂SiO₅ FET under different

back-gate voltages (V_{BG}) from 5 to 0 V. **f** The extracted threshold voltage V_{th} from **e** as a function of V_{BG}. The linear fitting yields a slope of −0.0097 and a high dielectric constant of ~32.3. **g** The thickness-dependent dielectric constant of Bi₂SiO₅ extracted by dual-gate measurement on Bi₂SiO₅/MoS₂/SiO₂/Si FET. The dotted curve is a visual guide. **h** Transfer curves of the MoS₂ FETs with different thickness Bi₂SiO₅ as the top-gate dielectrics, showing a trend of smaller V_{th} for thinner Bi₂SiO₅ thickness. The V_{ds} is 0.5 V, and no V_{BG} is applied. **i** Measured output voltage (V_{out}) and gain as a function of input voltage (V_{in}) of an NMOS inverter based on two MoS₂/ Bi₂SiO₅ FETs under different supply voltage (V_{dd}) from 2 V to 0.5 V.

within ±0.5 V, showing a low dynamic power consumption of <0.7 nW (Supplementary Fig. 26).

In summary, our work achieved the direct CVD growth of ultrathin free-standing high-*k* single-crystalline dielectrics, which is much more efficient than traditional mechanical exfoliation. The vertically grown Bi₂SiO₅ 2D crystals present the metrics for a gate dielectric, as evidenced by the coexistence of high dielectric constant, large band gap, high breakdown field strength, as well as the characteristic of easy transfer by facile polymer-free mechanical pressing. These features make Bi₂SiO₅ attractive as an inert vdWs substrate superior to *h*-BN for exploring exotic transport properties under reduced interfacial scatterings and stronger gate control, as well as for fabricating hysteresis-free 2D transistors with scaled supply voltage.

Methods

CVD growth of ultrathin Bi₂SiO₅ nanoplates on mica substrate
2D Bi₂SiO₅ crystals were synthesized inside a homemade CVD system equipped with a single heating zone tube furnace and 30 mm diameter quartz tube. Typically, the BiF₃ powders (purity 99.999%, Macklin)

were placed in an empty quartz boat or on top of the SiO₂ powders located in the heating center, and the freshly cleaved fluorophlogopite mica substrates were placed above the quartz boat. The heating temperature of the source was 600–750 °C and the growth time was 20 min. The 50 s.c.c.m Ar and 5 s.c.c.m mixed Ar/O₂ (1‰) gas were introduced into the CVD system as carrier gas. The system pressure was kept constant as 760 Torr during the whole growth process.

Characterization of CVD-grown ultrathin Bi₂SiO₅ single-crystalline dielectric
The morphologies of as-synthesized in-plane and free-standing 2D Bi₂SiO₅ nanoplates were characterized by optical microscopy (Olympus BX53), scanning electron microscopy (SEM, JSM-7800F) and atomic force microscope (AFM, Bruker dimension icon). With a polymer-free method of mechanical pressing, vertically grown Bi₂SiO₅ nanoflakes were transferred onto Cu grid, glass, and optical quartz substrates to perform the characterizations of transmission electron microscopy (TEM, JEM 2800), X-ray diffraction (XRD, Rigaku Smart Lab 30 KW) and absorption spectrum (SHIMADZU, UV-2600),

respectively. The Raman spectroscopy was measured on WITec alpha300R with a laser of 532 nm. The cross-sectional TEM samples of in-plane and vertically grown Bi_2SiO_5 nanoflakes were both prepared by using a focused ion/electron dual beam system (FEI, Helios 5 CX). All cross-sectional scanning transmission electron microscopy (STEM) imaging was obtained on an aberration-corrected TEM operating at 300 kV (FEI Titan cubed Themis G2 300). The breakdown field strength of Bi_2SiO_5 was measured with the C-AFM module of Bruker Dimension Icon.

First-principles calculations

The structural relaxation of Bi_2SiO_5 is performed within the framework of density function theory (DFT) using the projector augmented wave pseudopotential and the Perdew–Burke–Ernzerhof exchange-correlation functional as implemented in the VASP. The energy cut-off for the plane-wave expansion is set to 500 eV, and a Monkhorst–Pack k-mesh of $3 \times 9 \times 9$ is used in the Brillouin zone. The energy convergence threshold is 10^{-6} eV and the force 10^{-3} eV Å^{-1} in the structural optimization. In order to overcome the underestimation of energy gap from the generalized gradient approximation (GGA), we use the method of modified Becke–Johnson potential (mBJ) to calculate the electronic structure.

Device fabrication

To illuminate the possible capacitance coupling, the Bi_2SiO_5-based metal-insulator-metal (MIM) capacitors were fabricated on quartz substrates rather than SiO_2/Si substrates. First, the thick graphite was exfoliated onto the quartz substrate as bottom electrodes for its ultrasmooth surface. Next, the vertically grown Bi_2SiO_5 nanoflakes were directly picked up from the mica substrate by a polypropylene carbonate/polydimethylsiloxane (PPC/PDMS) stamp, followed by aligned transfer onto the specific graphite bottom electrode by a high-precision transfer platform. Subsequently, the standard electron-beam lithography (EBL) process and thermal evaporation were used to pattern the top electrodes ((In/Au, 5/40 nm).

For fabricating the back-gated MoS_2 Hall-bar device using graphite as bottom electrodes, the detailed process was listed as follows. First, SiO_2/Si substrates (285 nm SiO_2) were pretreated with O_2 plasma (Diener Pico plasma cleaner) for 5 min at a power of 50 W. Next, few-layer MoS_2 and graphite were exfoliated onto different SiO_2/Si substrates. With the help of the PPC/PDMS stamp and high-precision transfer platform, the free-standing Bi_2SiO_5 and MoS_2 nanoflakes were sequentially stacked on top of the graphite. The six-terminal electrode legs for the Hall-bar and the bottom metal electrodes were simultaneously written by one-step EBL and following thermal metal deposition (In/Au, 5/40 nm). The device fabrication process of 4-terminal MoS_2 FET includes the following parts: (1) transfer the Bi_2SiO_5 onto SiO_2/Si substrate by mechanical pressing; (2) place part of the few-layer MoS_2 on top of the Bi_2SiO_5 nanosheet; (3) EBL and metal deposition (In/Au, 5/40 nm).

For the top-gated MoS_2 device, few-layer MoS_2 nanosheets were exfoliated onto SiO_2/Si substrate, followed by stacking Bi_2SiO_5 nanoflakes in the middle of the MoS_2 nanosheets as the gate dielectrics. The source, drain, and top-gate electrodes of MoS_2 FETs were patterned together with one-step EBL process and thermal metal evaporation (In/Au, 5/40 nm).

Electrical transport measurements

2-probe electrical properties of the back-gate and top-gate MoS_2 FETs, including the Figs. 3e, f, 4b, 5b, c, e, h, were carried out by a semiconductor analyzer (FS-Pro) in a shielded vacuum chamber (<0.1 Torr) at room temperature, whose noise level is -1 $\times 10^{-13}$ A within the voltage range of ±2 V. The 4-probe transfer curves and gated 4-probe measurements (such as gated R_{xx}-T and Hall data), including Figs. 3b, d, 4c, were carried out in a Physical Properties Measurement Systems (PPMS-

9T, Quantum Design) equipped with a homemade electrical measurement system, which is composed of 2 Keithley 2400, and 2 Keithley 2182 A nanovoltmeter and has a noise level of -10^{-10} A within the voltage range of ± 2 V. The $C-V$ and $C-f$ measurements were carried out on a FS336 LCR Meter.

Data availability

Relevant data supporting the key findings of this study are available within the article and the Supplementary Information file. All raw data generated during the current study are available from the corresponding authors upon request.

References

1. Liu, Y. et al. Promises and prospects of two-dimensional transistors. *Nature* **591**, 43–53 (2021).
2. Jiang, J. et al. Ballistic two-dimensional InSe transistors. *Nature* **616**, 470–475 (2023).
3. Tan, C. et al. 2D fin field-effect transistors integrated with epitaxial high-k gate oxide. *Nature* **616**, 66–72 (2023).
4. Desai, S. B. et al. MoS_2 transistors with 1-nanometer gate lengths. *Science* **354**, 99–102 (2016).
5. Kang, K. et al. High-mobility three-atom-thick semiconducting films with wafer-scale homogeneity. *Nature* **520**, 656–660 (2015).
6. Das, S. et al. Transistors based on two-dimensional materials for future integrated circuits. *Nat. Electron.* **4**, 786–799 (2021).
7. Wang, S. Y. et al. Two-dimensional devices and integration towards the silicon lines. *Nat. Mater.* **21**, 1225–1239 (2022).
8. Yang, S. J. et al. Gate dielectrics integration for 2D electronics: challenges, advances, and oulook. *Adv. Mater.* **34**, 2207901 (2022).
9. Lin, Y. C. et al. Dielectric material technologies for 2-D semiconductor transistor scaling. *IEEE Trans. Electron Devices* **70**, 1454–1473 (2023).
10. Illarionov, Y. Y. et al. Insulators for 2D nanoelectronics: the gap to bridge. *Nat. Commun.* **11**, 3385 (2020).
11. Kim, H. G. et al. Atomic layer deposition on 2D materials. *Chem. Mater.* **29**, 3809–3826 (2017).
12. Xiao, M. M. et al. Atomic-layer-deposition growth of an ultrathin HfO_2 film on graphene. *ACS Appl. Mater. Interfaces* **9**, 34050–34056 (2017).
13. Li, N. et al. Atomic layer deposition of Al_2O_3 directly on 2D materials for high-performance electronics. *Adv. Mater. Interfaces* **6**, 1802055 (2019).
14. Illarionov, Y. Y. et al. Ultrathin calcium fluoride insulators for two-dimensional field-effect transistors. *Nat. Electron.* **2**, 230–235 (2019).
15. Huang, J. K. et al. High-k perovskite membranes as insulators for two-dimensional transistors. *Nature* **605**, 262–267 (2022).
16. Yang, A. J. et al. Van der Waals integration of high-k perovskite oxides and two-dimensional semiconductors. *Nat. Electron.* **5**, 233–240 (2022).
17. Jin, Y. et al. Controllable oxidation of ZrS_2 to prepare high-k, single-crystal m-ZrO_2 for 2D electronics. *Adv. Mater.* **35**, 2212079 (2023).
18. Zhang, C. C. et al. Single-crystalline van der Waals layered dielectric with high dielectric constant. *Nat. Mater.* **22**, 832–837 (2023).
19. Dean, C. R. et al. Boron nitride substrates for high-quality graphene electronics. *Nat. Nanotechnol.* **5**, 722–726 (2010).
20. Wang, L. et al. One-dimensional electrical contact to a two-dimensional material. *Science* **342**, 614–617 (2013).
21. Bandurin, D. A. et al. High electron mobility, quantum Hall effect and anomalous optical response in atomically thin InSe. *Nat. Nanotechnol.* **12**, 223–227 (2017).
22. Wu, S. F. et al. Observation of the quantum spin Hall effect up to 100 kelvin in a monolayer crystal. *Science* **359**, 76–79 (2018).
23. Yang, F. Y. et al. Quantum hall effect in electron-doped black phosphorus field-effect transistors. *Nano Lett.* **18**, 6611–6616 (2018).

24. Naclerio, A. E. et al. A review of scalable hexagonal boron nitride (h-BN) synthesis for present and future applications. *Adv. Mater.* **35**, 2207374 (2023).

25. Liu, K. L. et al. A wafer-scale van der Waals dielectric made from an inorganic molecular crystal film. *Nat. Electron.* **4**, 906–913 (2021).

26. Jin, Y. Y. et al. Growth of large-scale two-dimensional insulator $Na_2Ta_4O_{11}$ through chemical vapor deposition. *J. Semicond.* **41**, 072901 (2020).

27. Peng, J. et al. Inorganic low k cage-molecular crystals. *Nano Lett.* **21**, 203–208 (2021).

28. Zhu, C. Y. et al. 2D indium phosphorus sulfide ($In_2P_3S_9$): an emerging van der Waals high-k dielectrics. *Small* **18**, 2104401 (2022).

29. Han, M. J. et al. Continuously tunable ferroelectric domain width down to the single-atomic limit in bismuth tellurite. *Nat. Commun.* **13**, 5903 (2022).

30. Hong, C. Y. et al. Inclined ultrathin Bi_2O_2Se films: a building block for functional van der Waals heterostructures. *ACS Nano* **14**, 16803–16812 (2020).

31. Tan, C. W. et al. Strain-free layered semiconductors for 2D transistors with on-state current density exceeding 1.3 mA/μm^{-1}. *Nano Lett.* **22**, 3770–3776 (2022).

32. Park, J. et al. Tetrahedral tilting and ferroelectricity in Bi_2AO_5 (A=Si, Ge) from first principles calculations. *J. Solid State Chem.* **235**, 68–75 (2016).

33. Wu, Y. T. et al. Preparation and fluorescence property of pure Bi_2SiO_5 powders by Pechini sol-gel method. *Mater. Manuf. Process.* **32**, 480–483 (2017).

34. Liu, D. et al. Constructing a novel $Bi_2SiO_5/BiPO_4$ heterostructure with extended light response range and enhanced photocatalytic performance. *Appl. Catal. B* **236**, 205–211 (2018).

35. Depablos-Rivera, O. et al. Synthesis of Bi_2SiO_5 thin films by confocal dual magnetron sputtering-annealing route. *Thin Solid Films* **688**, 137258 (2019).

36. Taniguchi, H. et al. Ferroelectricity driven by twisting of silicate tetrahedral chains. *Angew. Chem. Int. Ed.* **52**, 8088–8092 (2013).

37. Kodera, M. et al. Ferroelectric properties of epitaxial Bi_2SiO_5 thin films grown on $SrTiO_3$ substrates with various orientations. *Jpn. J. Appl. Phys.* **58**, SLLB04-01 (2019).

38. Kijima, T. et al. Preparation of $Bi_4Ti_3O_{12}$ thin film on Si(100) substrate using Bi_2SiO_5 buffer layer and its electric characterization. *Jpn. J. Appl. Phys.* **37**, 5171–5173 (1998).

39. Sakamoto, K. et al. Fabrication of bismuth silicate Bi_2SiO_5 ceramics as a potential high-temperature dielectric material. *J. Mater. Sci.* **56**, 8415–8426 (2021).

40. Fisichella, G. et al. Interface electrical properties of Al_2O_3 thin films on graphene obtained by atomic layer deposition with an in situ seedlike layer. *ACS Appl. Mater. Interfaces* **9**, 7761–7771 (2017).

41. Chang, Y. C. et al. Atomic-layer-deposited Al_2O_3 and HfO_2 on GaN: a comparative study on interfaces and electrical characteristics. *Microelectron. Eng.* **88**, 1207–1210 (2011).

42. Mohanty, S. et al. Investigation and optimization of HfO_2 gate dielectric on N-polar GaN: Impact of surface treatments, deposition, and annealing conditions. *Appl. Phys. Lett.* **119**, 042901 (2021).

43. Ahmed, F. et al. Dielectric dispersion and high field response of multilayer hexagonal boron nitride. *Adv. Funct. Mater.* **28**, 1804235 (2018).

44. Kim, K. K. et al. Synthesis and characterization of hexagonal boron nitride film as a dielectric layer for graphene devices. *ACS Nano* **6**, 8583–8590 (2012).

45. Zhu, W. et al. Ternary VOCl single-crystal as efficient gate dielectric for 2D field-effect transistors. *2D Mater.* **8**, 025010 (2021).

46. Muller, D. A. et al. The electronic structure at the atomic scale of ultrathin gate oxides. *Nature* **399**, 758–761 (1999).

47. Stengel, M. et al. Origin of the dielectric dead layer in nanoscale capacitors. *Nature* **443**, 679–682 (2006).

48. Lu, Z. et al. Wafer-scale high-κ dielectrics for two-dimensional circuits via van der Waals integration. *Nat. Commun.* **14**, 2340 (2023).

49. Lin, H. C. et al. Leakage current and breakdown electric-field studies on ultrathin atomic-layer-deposited Al_2O_3 on GaAs. *Appl. Phys. Lett.* **87**, 182904 (2005).

50. Sire, C. et al. Statistics of electrical breakdown field in HfO_2 and SiO_2 films from millimeter to nanometer length scales. *Appl. Phys. Lett.* **91**, 242905 (2007).

51. Luo, P. F. et al. Molybdenum disulfide transistors with enlarged van der Waals gaps at their dielectric interface via oxygen accumulation. *Nat. Electron.* **5**, 849–858 (2022).

52. Yu, Z. H. et al. Realization of room-temperature phonon-limited carrier transport in monolayer MoS_2 by dielectric and carrier screening. *Adv. Mater.* **28**, 547–552 (2016).

53. Joo, M. K. et al. Understanding coulomb scattering mechanism in monolayer MoS_2 channel in the presence of h-BN buffer layer. *ACS Appl. Mater. Interfaces* **9**, 5006–5013 (2017).

54. Cui, X. et al. Multi-terminal transport measurements of MoS_2 using a van der Waals heterostructure device platform. *Nat. Nanotechnol.* **10**, 534–540 (2015).

55. Li, W. S. et al. Uniform and ultrathin high-k gate dielectrics for two-dimensional electronic devices. *Nat. Electron.* **2**, 563–571 (2019).

Acknowledgements

Author contributions
J.W. convinced the original ideas and supervised the whole project. J.C. performed the CVD growth, characterization, device fabrication, and electrical measurements under the assistance of Z.L., Y.L., Y.H., Y.D., and T.C. Z.G. assisted by Z.Z. performed part of the TEM characterizations. Z.L. plotted the cartoon diagram. X.D. performed the theoretical calculation under the supervision of H.F. J.W. and J.C. wrote the paper with the input of other authors. F.L. co-supervised the whole project and gave constructive suggestions. All authors contributed to the scientific discussions.

Competing interests
The authors declare no competing interest.

Additional information
Supplementary information The online version contains supplementary material available at https://doi.org/10.1038/s41467-023-40123-1.

Correspondence and requests for materials should be addressed to Jinxiong Wu.

Peer review information *Nature Communications* thanks Jing-Kai Huang and the other, anonymous, reviewer(s) for their contribution to the peer review of this work. A peer review file is available.

Reprints and permissions information is available at http://www.nature.com/reprints

Publisher's note Springer Nature remains neutral with regard to jurisdictional claims in published maps and institutional affiliations.